Solar Energy Materials and Solar Cells 184 (2018) 22–30

Contents lists available at ScienceDirect

Solar Energy Materials and Solar Cells

journal homepage: www.elsevier.com/locate/solmat

Hot corrosion behavior of commercial alloys in thermal energy storage material of molten $MgCl_2$/KCl/NaCl under inert atmosphere

Wenjin Ding[a,*], Hao Shi[b], Yanlei Xiu[a], Alexander Bonk[a], Alfons Weisenburger[b], Adrian Jianu[b], Thomas Bauer[c]

[a] Institute of Engineering Thermodynamics, German Aerospace Center (DLR), Stuttgart, Germany
[b] Institute for Pulsed Power and Microwave Technology, Karlsruhe Institute of Technology (KIT), Eggenstein-Leopoldshafen, Germany
[c] Institute of Engineering Thermodynamics, German Aerospace Center (DLR), Cologne, Germany

ARTICLE INFO

Keywords:
Concentrated solar power (CSP)
Hot corrosion
Impurity-driven corrosion
Molten salts
Chlorides

ABSTRACT

Hot corrosion behavior of three commercial alloys (stainless steel SS 310, Incoloy 800 H, Hastelloy C-276) in molten $MgCl_2$/NaCl/KCl (60/20/20 mol%) under inert atmosphere was investigated by immersion tests at 700 °C for 500 h. SS 310 exhibited the highest corrosion rate, while Hastelloy C-276 showed the best corrosion resistance. All the studied alloys could not meet the requirements for commercial application (i.e., corrosion rate < 10 μm/year for 30 year's lifetime). Microstructural analysis on the exposed alloy specimens using SEM, EDX and XRD shows that Cr was dissolved preferentially than Fe and Ni to form a corrosion layer with a porous structure during the corrosion. Moreover, the corrosion products (e.g., MgO, $MgCr_2O_4$, etc.) precipitated on the surface of the exposed specimens, as well as in the pores of the Cr-depleted corrosion layer. For SS 310 containing 2 wt% Si, Si was also dissolved and corrosion products containing Si were observed in the pores of the corrosion layer. Based on these findings, an impurity-driven corrosion mechanism is proposed to describe the hot corrosion behavior of the studied alloys in molten $MgCl_2$/NaCl/KCl under inert atmosphere, which could assist the development of corrosion mitigation technologies in future work.

1. Introduction

Concentrated solar power (CSP) technology is emerging as one important technology in the future renewable energy system. It is reported that global installed CSP-capacity has increased nearly fifteenfold from 2005 to 2015 (up to 4.8 Gigawatts) and grew at an average rate of 50% per year from 2010 to 2015 [1]. In CSP plants, storage of the heat from sunlight in thermal energy storage (TES) materials such as molten salts allows them to generate dispatchable power during the absence of sunlight and adds value of such power plants [2]. In commercial CSP plants, a non-eutectic salt mixture of 60 wt% sodium nitrate and 40 wt% potassium nitrate, commonly known as Solar Salt, is typically utilized as the TES material. The properties of commonly considered solar salts are listed in Table 1.

For power tower systems, it is desirable to raise the maximum operation temperature in order to increase the power block efficiency. This leads to reduced level of electricity costs. At present, two-tank molten salt storage is the only commercially available concept for CSP plants with a large thermal storage requirement [6]. This TES system can further be divided into the direct and indirect types. In a direct system, the salts work both as heat transfer fluid (HTF) and the storage medium, while in an indirect storage system, the thermal storage is decoupled from the HTF loop by the heat exchanger.

Table 2 gives detailed parameters about these direct and indirect two-tank molten salt TES systems with Solar Salt. Both systems have similar thermal capacities, but the tower system has much lower molten salt inventory. This is due to the fact that the thermal storage capacity of a molten salt is proportional to the temperature difference between the hot and cold tank. In other words, the large temperature difference between the cold and hot tank leads to a small sized TES system.

Since Solar Salt, listed in Table 1, decomposes at the temperatures around 550 °C, the temperature difference and the upper operation temperature of the TES system is limited [3]. In order to improve the power tower system performance, work on improving the stability of Solar Salt at high temperature has been done in our research group [7].

The current paper presents a new type of molten salts - molten chloride salts. Compared with the commercial molten nitrate salts used in CSP, this type of salts not only has high thermal stability (stable at above 800 °C) and relatively high heat capacity, but also a lower cost (Table 1). These advantages allow to operate them at temperature

* Corresponding author.
E-mail address: wenjin.ding@dlr.de (W. Ding).

https://doi.org/10.1016/j.solmat.2018.04.025
Received 1 December 2017; Accepted 23 April 2018
Available online 01 May 2018

Table 1
Properties of commonly used molten salts as TES materials in CSP.

Molten salts Composition (wt%)	Melting point (°C)	Stability limit (°C)	Heat capacity (kJ kg^{-1} K^{-1})	Cost ($/kg)
Solar Salt $NaNO_3/KNO_3$ (60/40)	240 [3]	530–565 [3]	1.55 (500 °C) [3]	0.5–1 [3]
Hitec $NaNO_3/KNO_3/NaNO_2$ (7/53/40)	142 [4]	535 [4]	1.56 (300 °C) [4]	0.7–1.1 [4]
ZnNaK chlorides $ZnCl_2$/NaCl/KCl (68.6/7.5/23.9)	204 [4]	850 [4]	0.81(300–600 °C) [4]	0.5–1 [4]
MgNaK chlorides $MgCl_2$/NaCl/KCl (68.2/14.0/17.8)	380 [2]	> 800 [5]	~1.0 (500–800 °C) [5]	< 0.5[a]

[a] Price of MgNaK chlorides is estimated with the approximate large-scale prices for all chloride salts.

Table 2
Commercial two-tank systems with Solar Salt [6].

	Direct storage	Indirect storage
CSP type	**Power tower**	**Parabolic trough**
System name	Gemasolar	Andasol 1
Thermal capacity	~ 1000 MWh	1010 MWh
Inventory	8500 tones	28500 tones
Cold tank temperature	290 °C	292 °C
Hot tank temperature	~565 °C	386 °C
Temperature difference	~275 °C	94 °C

above 600 °C, which means higher efficiency of thermal to electrical energy conversion [8]. Moreover, a larger temperature difference might lead to a small sized and cost effective TES system.

However, the application of molten chlorides at high temperatures causes additional challenges, particularly increased corrosiveness of metallic containers and structural materials [8–10]. Table 3 summarizes the corrosion rates (CR) of commercial Fe-Ni-Cr alloys in various molten salts under different conditions. It shows that even under inert atmosphere the super corrosion resistance Ni-based superalloys like Hastelloys C-22 and C-276, which are more expensive compare with SS 304, cannot meet in molten chlorides (e.g., $ZnCl_2$/KCl/NaCl at 800 °C) the requirements of corrosion resistance in commercial applications (CR < 10 μm/year for 30 year's lifetime). Gomez-Vidal and Tirawat [12] reported the severe corrosion (corrosion rates > 2000 μm/year) of selected alloys (SS 347, SS 310, In 800 H and In 625) in NaCl/LiCl (34.42/65.58 wt%) at 650 °C under nitrogen atmosphere. When the molten $MgCl_2$/NaCl/$CaCl_2$ is swept with the air, the Ni-based superalloys (e.g. Inconel 625, Hastelloys X and B-3) exhibit severe corrosion, even at 600 °C (CR > 100 μm/year) [11]. Immersion tests of Vignarooban et al. [9] show that the anaerobic CR value of Ha C-276 in $ZnCl_2$/NaCl/KCl is only 5 μm/year at 800 °C, whereas it reaches to 80 μm/year even at 500 °C in presence of air.

Table 3
Corrosion of Fe-Ni-Cr-based alloys in commonly used molten salts as TES materials.

Molten salts	Alloys	Ni (wt%)	T (°C)	Corrosion rate (μm/year)
Solar Salt	SS 316	10–14	600	15.9[a] [4]
	Ha 230	47–56	600	47[a] [4]
Hitec	SS 321	9–12	570	2[a] [4]
ZnNaK chlorides $ZnCl_2$/	SS 304	8–11	400	> 15[b] [9]
NaCl/KCl (68.6/7.5/	Ha C-22	~;56	400	~ 8[b] [9]
23.9 wt%)	Ha C-22	~ 56	800	~ 12[b] [9]
	Ha C-276	~ 57	500	~ 80[a] [9]
	Ha C-276	~ 57	400	~ 3[b] [9]
	Ha C-276	~57	800	~ 5[b] [9]
MgNaCa chlorides $MgCl_2$/	IN 625	~62	600	121[a] [11]
NaCl/$CaCl_2$ (14.95/	Ha X	~47	600	153[a] [11]
53.43/31.61 mol%)	Ha B-3	~65	600	145[a] [11]
NaLi chlorides NaCl/LiCl	SS 347	9–12	650	7490[b] [12]
(34.42/65.58 wt%)	SS 310	~20.5	650	6420[b] [12]
	In 800 H	30–35	650	5940[b] [12]
	IN 625	~62	650	2800[b] [12]

SS: Stainless steel; Ha: Hastelloy; IN: Inconel; In: Incoloy.
[a] In air.
[b] In inert atmosphere.

Besides the operating temperature and atmosphere, it is well accepted that impurities in molten chlorides have significant effect on corrosion rates of the alloys [2,13,14]. The impurities mainly come from the water and the oxygen existing in the chloride salts and/or the atmosphere above the salts [8]. Water in the chloride salts (e.g., strong hydrophilic chloride - $MgCl_2$), probably from hydrated phases and/or in the atmosphere, hydrolyzes following reactions (1) and (2) and produce corrosive impurities MgOHCl and HCl [15]. The hydrochloric acid reacts with the metallic containers and structural materials according to reaction (3), while oxygen containing species existing in the molten chloride salts (e.g. $MgOH^+Cl^-$, dissolved oxygen) corrode the containers and structural materials by oxidizing the alloying components as shown in the reactions (4) and (5) [11].

$$MgCl_2{\cdot}H_2O \rightarrow MgOHCl + HCl \quad (1)$$

$$MgCl_2{\cdot}H_2O \rightarrow MgO + 2HCl \quad (2)$$

$$xHCl + M \rightarrow MCl_x + (x/2)H_2 \quad (3)$$

$$xMgOH^+Cl^- + M \rightarrow xMgO + MCl_x + (x/2)H_2 \quad (4)$$

$$x/2O_2 + yM \rightarrow M_yO_x \quad (5)$$

M: alloying element, e.g., Cr.

Research efforts have been made to understand the corrosion mechanism of Fe-Ni-Cr-based alloys in molten chloride salts, e.g., $MgCl_2$/$CaCl_2$/NaCl [11] and $MgCl_2$/NaCl [16], but only under air conditions. As shown in Fig. 1, the combined effect of dissolution, oxidization and chlorination was considered in the corrosion mechanism of alloys in molten chlorides [11,16]. During the exposure, oxygen and water in air were continually dissolved in the molten chlorides and reacted with the molten chlorides to form corrosive HCl and Cl_2. These corrosive impurities can accelerate the corrosion of alloys, particularly the Cr element in the alloys, which has a strong electromotive force (EMF) in molten chlorides [17,18] and is very reactive to O_2, HCl and Cl_2 [11,16]. In this system, $CrCl_4$, $MgCr_2O_4$ and CrO_2Cl_2 are considered to be the main corrosion products.

Table 3 clearly shows the difficulty to control the corrosion rates of Fe-Ni-Cr-based alloys, exposed to molten chlorides under air atmosphere, below 10 μm/year (≥ 600 °C), due to the effect of O_2 and H_2O. Compared to air atmosphere, the alloys have much lower corrosion rates when exposed to the molten chlorides under inert atmosphere [9]. Besides, Ni-based alloys show better corrosion resistance than Fe-based steels. However, the prices of the materials also typically increase as Ni amount increases. However, there is still a lack of reliable data and research on the corrosion rates and mechanism of commercial Fe-Ni-Cr-based alloys in molten chlorides under inert atmosphere. Therefore, in order to realize the application of molten chlorides at high temperatures, it is important for corrosion mitigation, to study the corrosion behavior of commercial Fe-Ni-Cr-based alloys exposed to molten chlorides under inert atmosphere.

In this work, three commercial Fe-Ni-Cr-based alloys (SS 310, Incoloy 800 H, Hastelloy C-276) are selected. Since the prices of MgNaK chlorides are lower than ZnNaK chlorides, immersion tests were performed in molten $MgCl_2$/NaCl/KCl (60/20/20 mol%) under argon

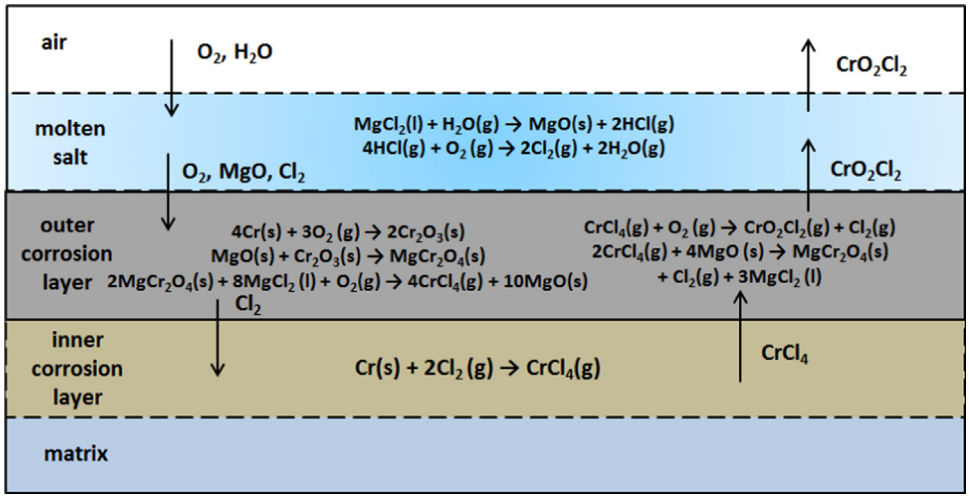

Fig. 1. Schematic diagram showing corrosion mechanism of Fe-Ni-Cr -based alloys in molten $MgCl_2/CaCl_2/NaCl$ under air atmosphere [11].

Table 4
Chemical composition of the studied alloys (wt%), EMF(V): theoretical standard electromotive forces of element in chloride salts [21].

Alloy	Fe	Ni	Cr	Mn	Si	Mo	C	W
SS 310	Balance	19–22	24–26	2	1.75	…	0.25	…
In 800	Balance	30.52	20.47	0.58	0.50	…	0.07	…
Ha C-276	6.20	Balance	15.81	0.40	0.03	15.47	0.004	3.57
EMF (V)	$1.12_{800\ °C}$	$0.88_{800\ °C}$	$1.35_{800\ °C}$	$1.81_{800\ °C}$	$1.47_{100\ °C}$	$0.47_{550\ °C}$	$0.15_{100\ °C}$	$0.43_{300\ °C}$

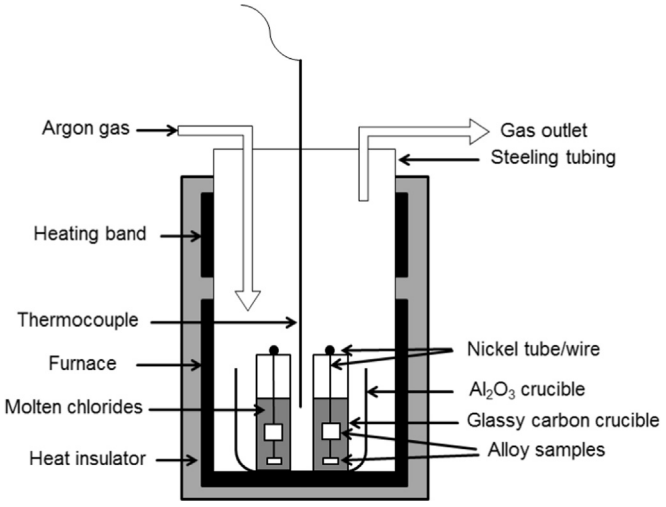

Fig. 2. Schematic diagram of experimental set-up for immersion tests in molten $MgCl_2/KCl/NaCl$.

atmosphere at 700 °C for 500 h. After exposure, the corrosion behavior of these alloys were evaluated by the mass loss method, X-ray diffraction (XRD) and scanning electron microscope (SEM) characterization methods. Based on the obtained results, the corrosion mechanism is also discussed.

2. Experimental

2.1. Chemicals and investigated alloys

KCl(*Alfa Aesar*, > 99%), NaCl(*Alfa Aesar*, > 99%) and anhydrous $MgCl_2$(*Magnesia*, > 99%, technical grade) were used to synthesize the salt mixture of $MgCl_2/KCl/NaCl$ (60/20/20 mol%). Referring to previous results [15], the heating of the salts were conducted as following: after vacuuming (≤ 30 mbar), the salt mixture was heated under argon atmosphere (purity ≥ 99.9999%, $H_2O \leq 0.5$ ppm, 20 l/h (STP), the absolute pressure above the salts is ~1.1 bar) from room temperature to 200 °C with a heating rate of 5 °C/min, then kept at 200 °C for 1 h to remove residual water in the hygroscopic $MgCl_2$ salt. After that, it was heated to 700 °C and kept at this temperature for corrosion tests with the immersed specimens. The measurements of titration and cyclic voltammetry (CV), which are described in our previous works [19,20], show that the concentration of the corrosive impurity $MgOH^+$ in the salts after the heating process was ~2000 ppm (5×10^{-2} mol/kg(salt)) at 700 °C.

Table 4 summarizes the chemical compositions of the alloys used in this study, and the theoretical standard electromotive forces (EMF) of the main elements in these alloys in their chloride salts [21]. The higher the EMF value is, the more reactive the element is. SS 310 has the highest proportion of "reactive elements" Cr, Fe, Mn and Si (high EMF), whereas Ha C-276 has a high content of Ni, which has a lower theoretical EMF than Cr, Fe, Mn and Si.

2.2. Immersion tests

Fig. 2 shows a schematic of the experimental set-up used for immersion tests in molten chlorides. High temperature resistant glassy carbon crucibles purchased from HTW Germany (Sigradur® G, GAZ 4) were used to avoid any reaction of the molten salts with the crucible. During the experiments, the temperature of the molten salts under an argon atmosphere (same parameters mentioned in Section 2.1.) was controlled by a thermocouple closed to the crucible. As shown in Fig. 2, in a glassy carbon crucible with a diameter of 30 mm and a height of 107 mm (open on the top), two pieces of each alloy (larger: 10 mm × 10 mm × 10 mm, smaller: 3 mm × 10 mm × 10 mm) were hung via a Nickel wire and completely immersed in the molten $MgCl_2/NaCl/KCl$ (60/20/20 mol%, 150 g). Before tests, all samples were grinded by sandpapers (600, 800 and 1200#), and washed by distilled water and acetone. In order to ensure that all the surfaces of the specimen are in full contact with the molten chlorides, they are hanged up by a nickel wire on a nickel tube cross on the glassy carbon crucible. After 500 h

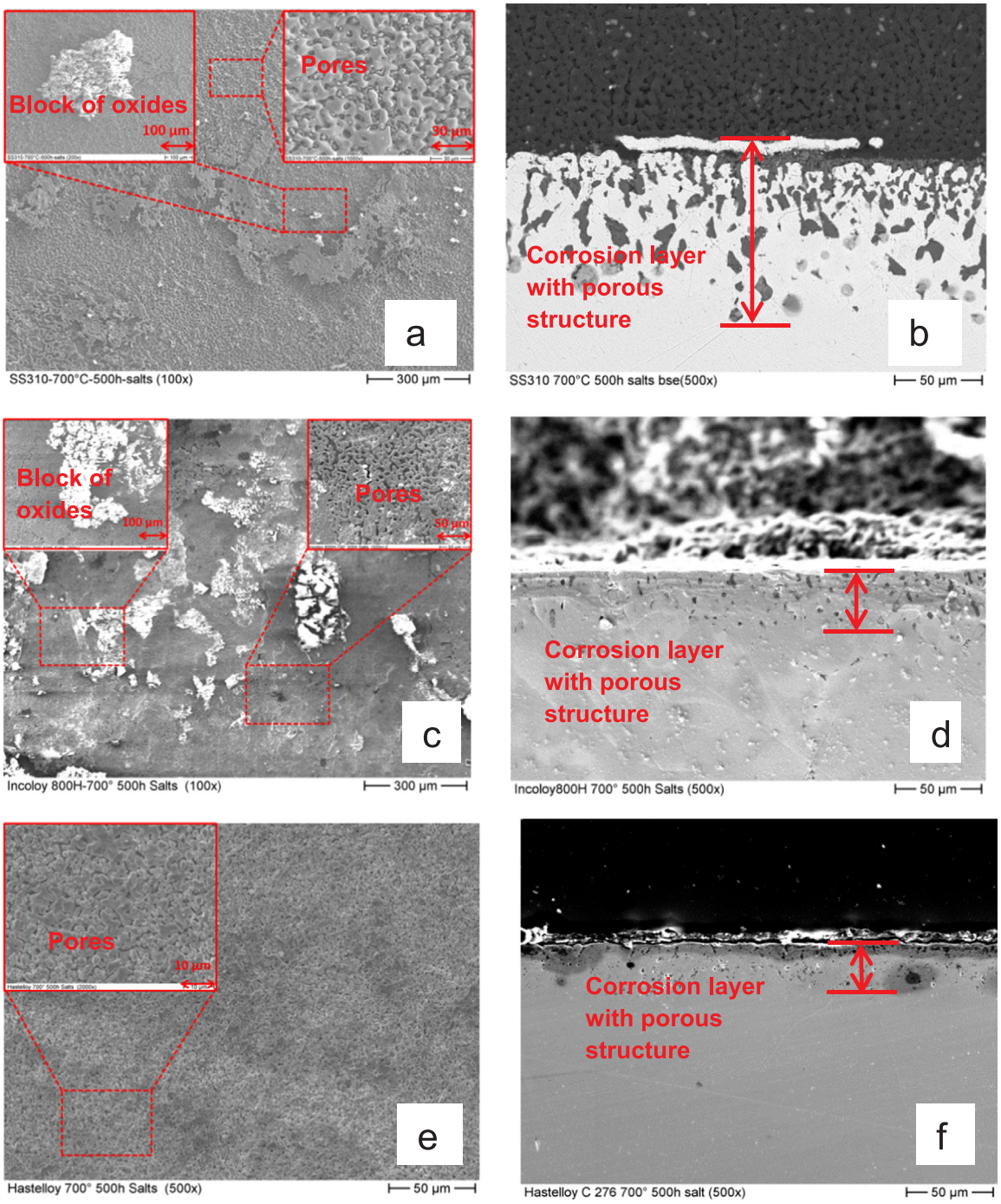

Fig. 3. SEM surface and cross-section images of SS 310 (a and b), In 800H (c and d) and Ha C-276 (e and f) after exposure to molten $MgCl_2$/KCl/NaCl at 700 °C for 500 h.

exposure, the furnace was cooled down to room temperature under argon atmosphere. The larger piece was used to measure the corrosion rate, with the mass loss method and the smaller one was used for microstructural analysis.

2.3. Corrosion analysis

2.3.1. Mass loss method

According to ASTM G1–03 [22], the exposed SS 310 specimens were washed with a nitric acid reagent (a mixture of 100 ml 70 wt% HNO_3, and 900 ml distilled water) at 60 °C for 20 min, while the exposed specimens of In 800H and Ha C-276 were washed with a hydrochloric acid reagent (a mixture of 150 ml 37 wt% HCl and 850 ml distilled water) at room temperature for 3 min. This process was repeated several times until the weight of the specimen did not change. Finally, they were cleaned again with acetone and dried with cold air. The specimens were weight by an electronic balance (*Mettler Toledo* AG245, accuracy of 0.1 mg) before and after corrosion tests. Under the assumption of uniform corrosion, the corrosion rates were calculated based on the following Eq. (6) [16,22]:

$$CR(\mu m/year) = \frac{K \cdot W}{A \cdot t \cdot \rho}, \quad (6)$$

where K is a factor (8.76×10^7 μm/y); W is the mass loss of the

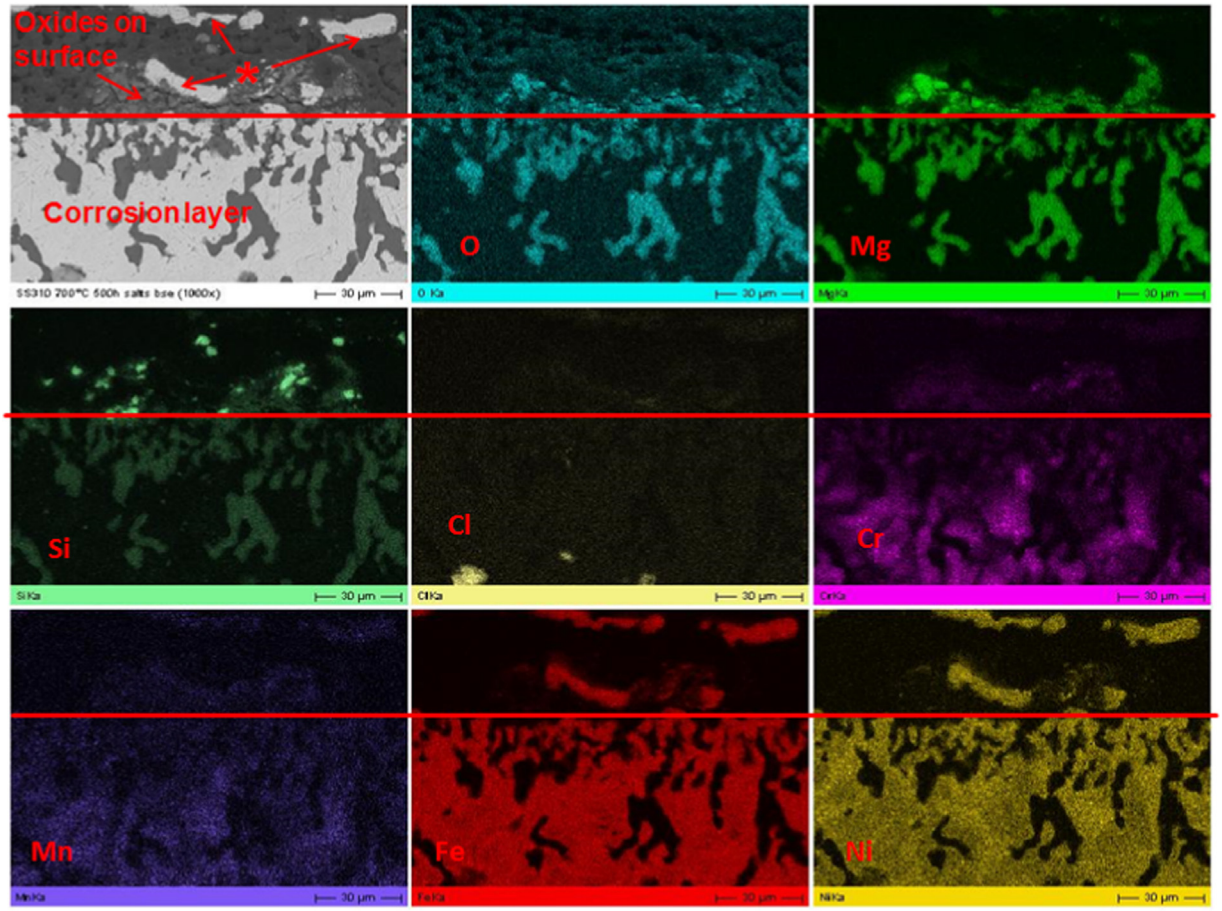

Fig. 4. Cross-section SEM and EDX elemental maps of corroded SS 310 after immersion in molten $MgCl_2$/KCl/NaCl (60/20/20 mol%) at 700 °C for 500 h. *: small Cr-depleted alloy pieces spalled off.

specimen due to the corrosion (g); A is the specimen area (cm^2); *t* is the immersion time of the specimen in molten salts (hour); ρ is the specimen density (g/cm^3). The densities of SS 310, In 800H and Ha C-276 are 7.89 g/cm^3, 7.95 g/cm^3 and 8.89 g/cm^3, respectively.

2.3.2. *Microstructural analysis*

In order to analyze the microstructure of the specimens after corrosion tests, the salt deposit on the surface of the specimens was carefully removed with a small brush to keep the corrosion products (i.e., oxides) remaining on the surface. On the surface and cross section of the specimens, complimentary techniques like scanning electron microscopy (SEM), energy-dispersive X-ray spectroscopy (EDX) were employed. SEM–EDX examination was performed with Philips XL40 equipped with a SAMx–EDX system. Moreover, the phase composition of the corrosion products was analyzed using a Seyfert C3000 powder diffractometer (Cu Kα radiation) with θ–2θ conventional geometry.

3. Results

After immersion in $MgCl_2$/KCl/NaCl at 700 °C for 500 h, the corrosion rates of the tested alloys were calculated according to Eq. (6). The calculated corrosion rates of SS 310, In 800H and Ha C-276 are 1581, 364 and 79 μm/year, respectively. The super-alloy Ha C-276 showed the best corrosion resistance.

Porous alloy surfaces can be observed by analyzing the SEM images of the exposed specimens like depicted in Fig. 3. This implies a selective corrosion of elements in the studied alloys, when exposed to molten chlorides salts. Moreover, there were some blocks of oxides precipitated on the surface of SS 310 and In 800H, which cannot be found on the surface of Ha C-276, as shown in Fig. 3(a), (c) and (e). EDX measurements of these blocks indicated that they were composed of O, Mg and Cr (not shown in this work). Other elements from alloys such as Fe and Ni were not detected.

Cross-section SEM images presented in Fig. 3(b), (d) and (f) show that the thickness of the corrosion layers of SS 310, In 800 H and Ha C-276 is 100, 50 and 30 μm after 500 h immersion at 700 °C, respectively. Accordingly, the corrosion rates calculated based on the corrosion layer are 1752, 876 and 526 μm/year, respectively. Cross-section EDX measurements show that Cr was dissolved from the alloys yielding a corrosion layer with porous structure (shown in Fig. 3(b), (d) and (f), Figs. 4–6). In the pores of the corrosion layer, Mg and O were detected by EDX (Figs. 4–6). In case of Ha C-276 also Cr, alongside with Mg and O, was observed in the pores located close to the specimen surface (Fig. 6), while in case of In800H the corrosion products containing Mg, Cr and O were detected mainly on the sample surface (Fig. 5). Beside Cr also Si was dissolved from the bulk SS 310 steel, as Si has an EMF value close to that of Cr at 700 °C (see Table 4), and was detected on the surface of the specimen and in the pores of the corrosion layer (Fig. 4). Thus, the corrosion products of SS 310 contain additionally Mg-Si-based oxides, e.g., $MgSiO_3$.

Interestingly, in case of SS 310 and In 800 H, it was observed from the EDX maps of Fe and Ni in Fig. 4 and Fig. 5, that some small Cr-depleted alloy pieces spalled off from the alloy surface during the exposure.

All exposed samples were examined by XRD (*θ-2θ*) Fig. 7)). In case of SS310, it was concluded from XRD pattern that the corrosion products were MgO, $MgCr_2O_4$ and $MgSiO_3$ (Fig. 7a). After removing some micrometers from the surface of this sample, this newly-obtained XRD

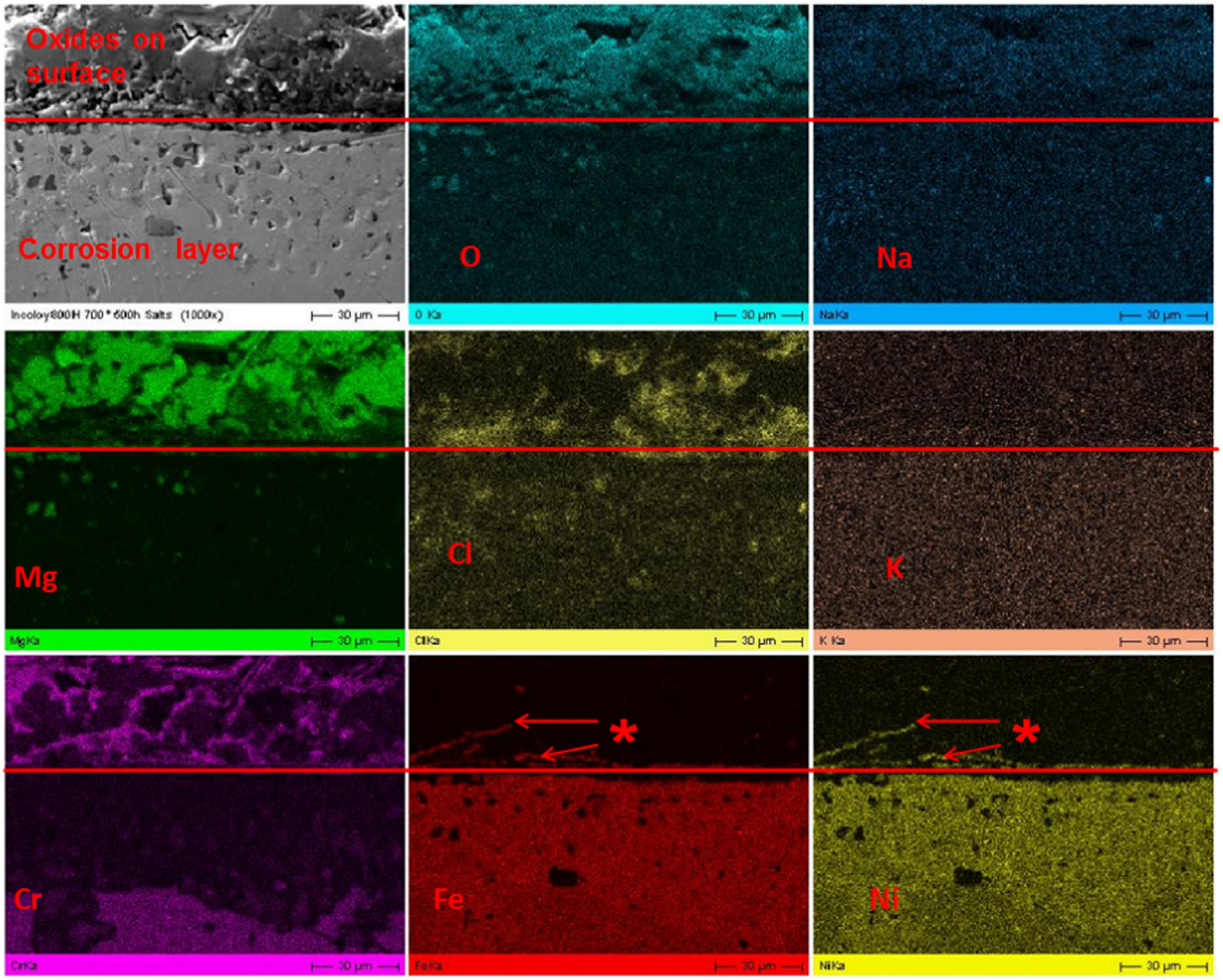

Fig. 5. Cross-section SEM and EDX elemental maps of corroded In 800H after immersion in molten $MgCl_2$/KCl/NaCl (60/20/20 mol%) at 700 °C for 500 h. *: small Cr-depleted alloy pieces spalled off.

pattern show that the corrosion products precipitated in the pores of the corrosion layer were MgO and $MgSiO_3$ (Fig. 7b). The XRD pattern of the In 800 H alloys proofs the presence of two oxides MgO and $MgCr_2O_4$ (Fig. 7c), while in case of Ha C-276 only the peaks corresponding to $MgCr_2O_4$, as corrosion products, were observed (Fig. 7d).

4. Discussion

Table 5 summarizes the corrosion rates at 700 °C of the studied alloys obtained using the mass loss and microstructural investigation method. All the studied alloys could not meet the requirements for commercial application (corrosion rates < 10 μm/year). Compared to the CR determined by the mass loss method, the CR determined from the microstructural investigation are higher, which can be explained by the selective corrosion. Only Cr and Si are removed from the matrix to form this porous structure in the corrosion layer. Fig. 8 shows the relations between the mass fractions of Ni, Cr and Fe elements in the studied alloys and the corrosion rates. Ha C-276, which has the highest content of Ni (~58 wt%) and lower Cr (~16 wt%), exhibits the best corrosion resistance. In contrast, SS 310, which contains 24 wt% Cr and only 20 wt% Ni, shows the poorest corrosion resistance.

The appearance of Cr-enriched precipitates mainly at the surface of the exposed alloys, and less in the pores of the corrosion layer, may be explained by considering that $CrCl_2$ produced in the pores of the corrosion layer during the corrosion was dissolved in the molten salt, then diffused out and reacted with the Mg^{2+} and O^{2-} in the bulk molten salt further to $MgCr_2O_3$ on the specimen surface. This led to the enrichment of Cr-containing corrosion products on the surfaces of the alloys. More details can be found in the proposed corrosion mechanism below, shown in Fig. 9.

All the facts in the results section imply that Cr in the alloys (and Si in SS 310) is dissolved preferentially than Fe and Ni, which causes the selective corrosion. Moreover, it seems that Cr and Si in the grains diffuses to the grains boundary at elevated temperature. Then, in form of inter-granular corrosion, they react with the corrosive impurities from the molten salt. Thus, the corrosion of Fe-Ni-Cr-based alloys in molten chlorides observed in our experimental conditions is selective and inter-granular.

With the collected information from the microstructure evolution of the exposed alloys, a model of impurity-driven corrosion mechanism is proposed (Fig. 9). Since in this work the atmosphere above molten salt is inert (i.e., swept with Ar with purity ≥ 99.9999%, H_2O ≤ 0.5 ppm), only the corrosive impurities from molten salt are considered. In our previous works, it was shown in cyclic voltammograms that $MgOH^+$ ion is the most stable and likely corrosive impurity in molten $MgCl_2$/KCl/NaCl under inert atmosphere [19,20]. It can be produced by hydrolysis of water adsorbed in the chloride salts during the heating (see reaction (1)). We assume that no reaction occurs in the molten $MgCl_2$/KCl/NaCl and no HCl gas above the salt is swept out, which means that the molten $MgCl_2$/KCl/NaCl keep an equilibrium, shown in reaction (7). Therefore, the concentrations of the $MgOH^+$, Mg^{2+}, O^{2-} and H^+ ions are constant.

$$MgOH^+ \leftrightarrow Mg^{2+} + O^{2-} + H^+ \quad (7)$$

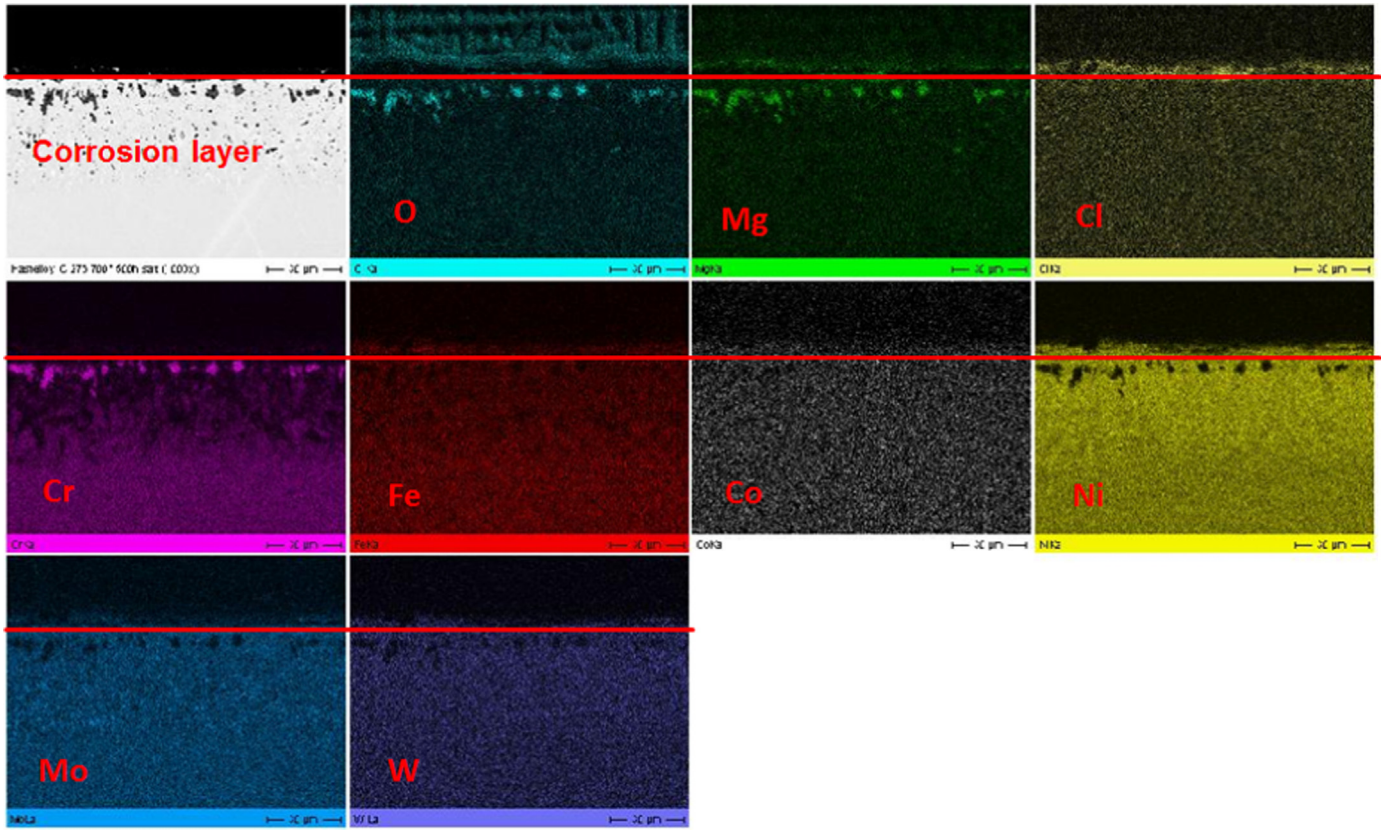

Fig. 6. Cross-section SEM and EDX elemental maps of corroded Ha C-276 after immersion in molten $MgCl_2$/KCl/NaCl (60/20/20 mol%) at 700 °C for 500 h.

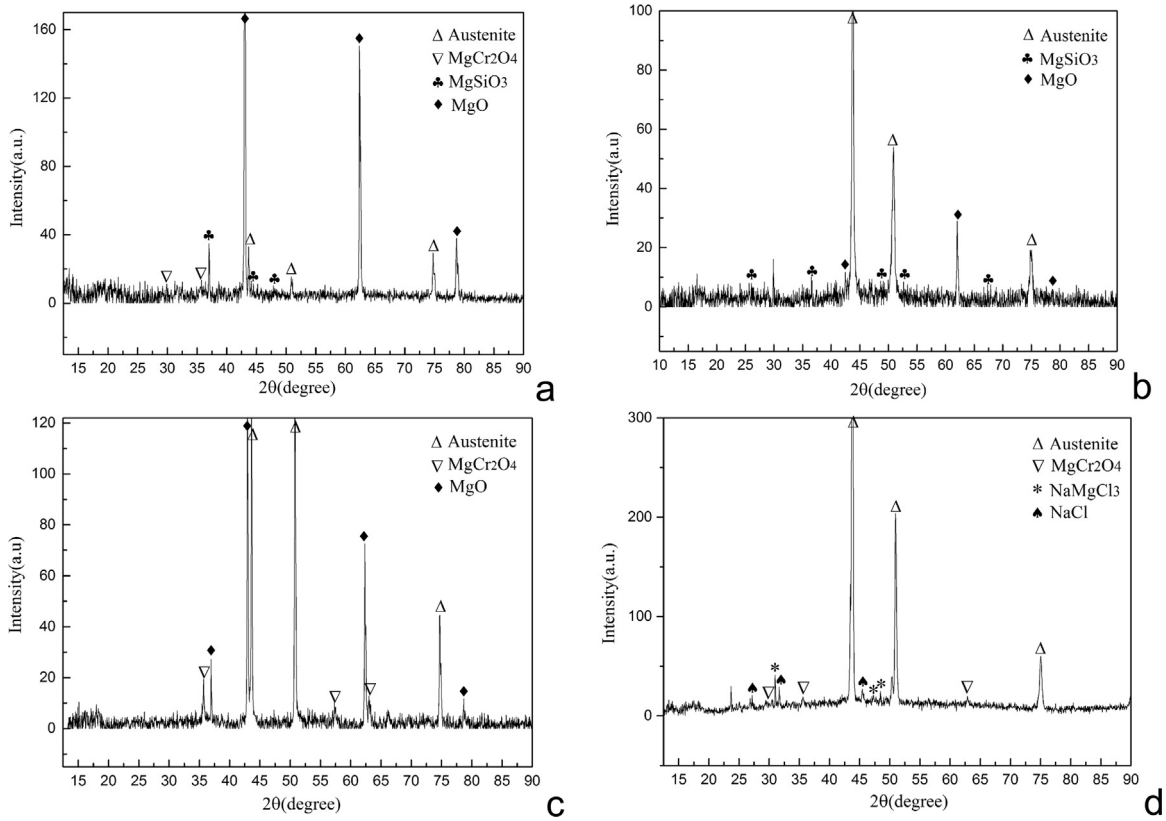

Fig. 7. XRD patterns of the exposed specimens, containing the peaks of the corrosion products on their surface: a) SS 310; c) In 800H; d) Ha C-276 and inside the pores of SS 310 (b). Austenite is the main structural phase of the studied alloy, while KCl, NaCl and $NaMgCl_3$ are the salts remaining on the alloy surface.

Table 5
Corrosion rates of the studied alloys in molten chlorides at 700 °C (calculated from mass loss method and microstructural investigation).

Alloys	SS 310	In 800 H	Ha C-276
CR (μm/year) mass loss	1581	364	79
CR (μm/year) microstructure	1752	876	526

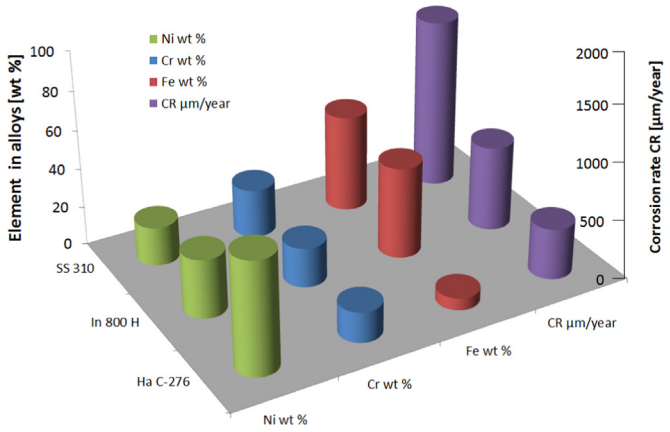

Fig. 8. Comparison of mass fractions of Ni, Cr and Fe elements in alloys SS 310, In 800 H and Ha C-276, and corrosion rates determined from microstructural investigation.

As shown in reaction (8) and Fig. 9, when the atmosphere above the molten salt is swept with an inert gas, HCl gas dissolved in the molten salts is swept out due to its low solubility (2.5×10^{-2} mol/kg in molten $MgCl_2$/KCl 50/50 mol% under 1 atm HCl at 700 °C [23]).

$$H^+ + Cl^- \rightarrow HCl\ (g) \quad (8)$$

Results from Laitinen et.al [24] shows that the hydrogen electrode potential, in eutectic LiCl/KCl molten salt at 450 °C, varies in the range of − 0.6 and − 1.0 V (vs. reference electrode Pt^{2+}/Pt), when HCl has a partial pressure of 0.02–0.9 bar in the gas above the molten salt. By comparing this value with the electrode potential of Cr in molten $MgCl_2$/KCl/NaCl at 475 °C (see Table 6), and considering the electromotive forces of Cr and Si (see Table 4), it can be concluded that H^+ ion in the molten salt will react with Cr and Si from the alloys. The reactions can be written as following: reactions (9 and 10). Fe and Ni are more resistant in molten $MgCl_2$/KCl/NaCl salts probably due to the low

Table 6
Standard electrode potentials in molten $MgCl_2$/KCl/NaCl (50/20/30 mol%) at 475 °C [25].

Electrode system	Cr^{2+}/Cr	Fe^{2+}/Fe	Cr^{3+}/Cr	Ni^{2+}/Ni
E°_m Vs. Pt^{2+}/Pt (V)	− 1.396	− 1.183	− 1.131	− 0.792

electromotive forces.

$$2H^+ + Cr \rightarrow Cr^{2+} + H_2(g) \quad (9)$$

$$4H^+ + Si \rightarrow Si^{4+} + 2H_2(g) \quad (10)$$

As the concentration of H^+ decreases due to the reaction with the alloys or the escape of HCl from the molten salt into the sweep gas, the equilibrium in reaction (7) shifts to the right side, and the concentrations of Mg^{2+} and O^{2-} in the molten salt increase. This leads to the formation of MgO as observed in reaction (11), which precipitates due to its low solubility (~2000 ppm, i.e., 5×10^{-2} mol/kg(salt, in $MgCl_2$/NaCl 60/40 mol% at 730 °C [26,27]).

$$Mg^{2+} + O^{2-} \rightarrow MgO(s) \quad (11)$$

Such MgO precipitates have been observed on the bottom of the glassy carbon crucible, in the pores of the corrosion layer and also on the surface of the alloy specimens (Figs. 4–6). Besides MgO particles, Mg^{2+}, O^{2-}, Cr^{2+} and Si^{4+} can also form some stable Mg-Cr-O according to reaction (12) (e.g., $MgCr_2O_3$, which was oxidized to $MgCr_2O_4$ in air according to reaction (13)) and Mg-Si-O precipitates (e.g., $MgSiO_3$) according to reaction (14). These precipitates also have been detected on the surface of the specimens and in the pores of the corrosion layers.

$$Mg^{2+} + 2\ Cr^{2+} + 3\ O^{2-} \rightarrow MgCr_2O_3(s) \quad (12)$$

$$\text{in air: } 2\ MgCr_2O_3(s) + O_2 \rightarrow 2\ MgCr_2O_4(s) \quad (13)$$

$$Mg^{2+} + Si^{4+} + 3\ O^{2-} \rightarrow MgSiO_3(s) \quad (14)$$

In general, the corrosion of alloys is controlled by the kinetics of the electron transfer reaction at the alloy surface [28]. Both, experiment and simulation, have proved that the corrosion reactions of Ni-based alloys (e.g., Ha 230) were controlled by electron transfer when exposed to molten KCl-$MgCl_2$ at 700–1000 °C [29,30]. Moreover, the corrosion rate of Ha 230 had a linear increase with corrosive species in the molten KCl-$MgCl_2$ [29,30]. In this work, it can be assumed for the corrosion mechanism proposed above that corrosion reactions (9) and (10) are controlled by the kinetics of the electron transfer reaction at the alloy

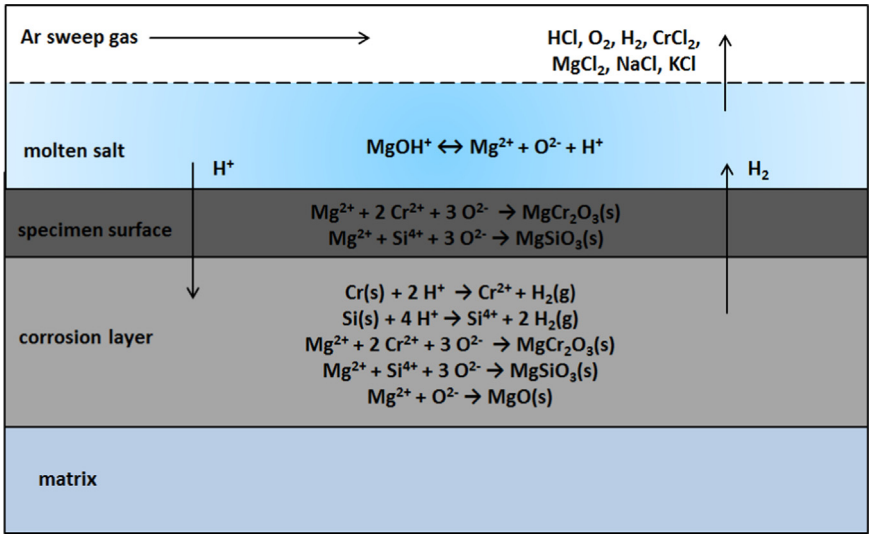

Fig. 9. Schematic diagram of the corrosion mechanism of Fe-Ni-Cr based alloys in molten $MgCl_2$/KCl/NaCl under inert atmosphere.

surface. Thus, the corrosive species H^+ has the same concentration in the bulk melt and at the surface of the alloys. Moreover, as $MgOH^+$ has been observed to be the most stable impurity in the melt, the impurity-driven corrosion reactions (9) and (10) are controlled by the slow shifting of the reaction (7) to the right side (producing the corrosive species H^+). Thus, we propose that the impurity-driven corrosion rate of Fe-Ni-Cr-based alloys in molten chlorides can be described with the following function, which is based on the concentration of the corrosive impurity $MgOH^+$:

$$CR\ (\mu m/\text{year}) = k(T)\cdot c(MgOH^+)^a\,, \quad (15)$$

where k(T) is the reaction constant in μm/year/(ppm) depending on the temperature of the melt, $c(MgOH^+)$ represents the concentration of the corrosive impurity $MgOH^+$ in the salts in ppm and a is the reaction order.

Based on the corrosion mechanism proposed in Fig. 9, the future work will focus on determining the kinetic parameters of the corrosion process and on developing corrosion mitigation technologies. The concentration of $MgOH^+$ will be measured by titration and cyclic voltammetry (CV) [19,20]. The kinetic parameters in Eq. (15) (k(T) and a), which describe the corrosion rate at different temperatures, will be determined by fitting the measured CRs with the concentration of the corrosive impurity $MgOH^+$. Then the allowed concentration of the corrosive $MgOH^+$ in molten $MgCl_2$/NaCl/KCl can be estimated. As for corrosion mitigation strategies, we propose (i) to control the concentration of corrosive $MgOH^+$ and H^+ ions in the molten salt, by adding some corrosion inhibitors such as Mg [31] and (ii) to develop materials able to form protective surface layers.

5. Conclusions

The corrosion behavior of three selected commercial Fe-Cr-Ni-based alloys (SS 310, Incoloy 800 H, Hastelloy C-276) was investigated in molten $MgCl_2$/NaCl/KCl (60/20/20 mol%) under inert atmosphere at 700 °C for 500 h.

The main conclusions of this work are:

- SS 310 has the highest corrosion rate, while Hastelloy C-276 has the best corrosion resistance
- The corrosion of the alloys was selective and inter-granular. During the corrosion experiments, Cr (Si in SS 310) was preferentially corroded, resulting a porous surface layer. The main corrosion products were found preferably either on the surface in case of the Cr-containing, or in the pores in case of Si-containing.
- The corrosion of the alloys is impurity-driven: the corrosive impurity $MgOH^+$ in the salts reacts with Cr and Si in the alloys.
- All the studied alloys could not meet the requirements for commercial applications (< 10 μm/year).

Acknowledgments

This research has been performed within the DLR-DAAD fellowship program, which is funded by German Academic Exchange Service (DAAD) and German Aerospace Center (DLR) (Grant Number: 57265854). The authors would like to thank Markus Braun, Jochen Forstner and Ulrike Kröner at the DLR-Institute of Engineering Thermodynamics for their technical support.

References

[1] REN21, Renewables 2016: Global Status report. ISBN 978-3-9818107-0-7, 2016.
[2] Y. Tian, C.Y. Zhao, A review of solar collectors and thermal energy storage in solar thermal applications, Appl. Energy 104 (2013) 538–553.
[3] T. Bauer, N. Pfleger, D. Laing, W.-D. Steinmann, M. Eck, S. Kaesche, High-temperature molten salts for solar power application (Chapter 20), in: F.L. Groult (Ed.), Molten Salts Chemistry, Elsevier, Oxford, 2013, pp. 415–438.
[4] K. Vignarooban, X. Xu, A. Arvay, K. Hsu, A.M. Kannan, Heat transfer fluids for concentrating solar power systems – a review, Appl. Energy 146 (2015) 383–396.
[5] Y. Li, X. Xu, X. Wang, P. Li, Q. Hao, B. Xiao, Survey and evaluation of equations for thermophysical properties of binary/ternary eutectic salts from NaCl, KCl, $MgCl_2$, $CaCl_2$, $ZnCl_2$ for heat transfer and thermal storage fluids in CSP, Sol. Energy 152 (2017) 57–79.
[6] T. Bauer, N. Breidenbach, Overview of Molten Salt Storage Systems and Material Development for Solar Thermal Power Plants, World Renewable Energy Forum, Denver, Colorado, USA, 2012.
[7] A. Bonk, C. Martin, M. Braun, T. Bauer, Material investigations on the thermal stability of Solar Salt and potential filler materials for molten salt storage, in: Proceedings of the 22nd SolarPACES Conference, October 2016, Abu Dhabi, UAE.
[8] A.M. Kruizenga, Corrosion Mechanisms in Chloride and Carbonate Salts, SANDIA Report SAND2012-7594, 2012.
[9] K. Vignarooban, X. Xu, K. Wang, E.E. Molina, P. Li, D. Gervasio, A.M. Kannan, Vapor pressure and corrosivity of ternary metal-chloride molten-salt based heat transfer fluids for use in concentrating solar power systems, Appl. Energy 159 (2015) 206–213.
[10] J.C. Gomeyz-Vidal, A.G. Fernandez, R. Tirawat, C. Turchi, W. Huddleston, Corrosion resistance of alumina-forming alloys against molten chlorides for energy production.I Pre-oxidation treatment and isothermal corrosion tests, Sol. Energy Mater. Sol. Cells (2017) 222–233.
[11] B. Liu, X. Wei, W. Wang, J. Lu, J. Ding, Corrosion behavior of Ni-based alloys in molten NaCl-$CaCl_2$-$MgCl_2$ eutectic salt for concentrating solar power, Sol. Energy Mater. Sol. Cells 170 (2017) 77–86.
[12] J.C. Gomez-Vidal, R. Tirawat, Corrosion of alloys in chloride molten salt (NaCl-LiCl) for solar thermal technologies, Sol. Energy Mater. Sol. Cells 157 (2016) 234–244.
[13] G.Y. Lai, High-temperature Corrosion and Materials Applications, Chapter 15 in book: Molten Salt Corrosion, ASM International, 2007.
[14] H.R. Copson, Corrosion of heating electrodes in molten chloride baths, J. Electrochem. Soc. 100 (6) (1953) 257–264.
[15] L. Maksoud, T. Bauer, Experimental investigation of chloride molten salts for thermal energy storage applications, in: Proceedings of the 10th International Conference on Molten Salt Chemistry and Technology, 10–12 June, Shenyang, China, 2015.
[16] J.W. Wang, C.Z. Zhang, Z.H. Li, H.X. Zhou, J.X. He, J.C. Yu, Corrosion behavior of nickel-based superalloys in thermal storage medium of molten eutectic NaCl-$MgCl_2$ in atmosphere, Sol. Energy Mater. Sol. Cells 164 (2017) 146–155.
[17] H.C. Gaur, W.K. Behl, Electrode potentials in fused magnesium chloride-sodium chloride-potassium chloride eutectic, Electrochim. Acta 8 (1963) 107–114.
[18] H.A. Laitinen, C.H. Liu, An electromotive force series in molten lithium chloride-potassium chloride eutectic, JACS 80 (1958) 1015–1020.
[19] W. Ding, A. Bonk, J. Gussone, T. Bauer, Cyclic voltammetry for monitoring corrosive impurities in molten chlorides for thermal energy storage, Energy Procedia 135 (2017) 82–91.
[20] W. Ding, A. Bonk, J. Gussone, T. Bauer, Electrochemical method for monitoring corrosive impurities in molten $MgCl_2$/KCl/NaCl salts for thermal energy storage, in: Proceedings of the 11th International Renewable Energy Storage Conference (IRES 2017) Düsseldorf Germany, 2017.
[21] W.J. Hamer, M.S. Malmberg, B. Rubin, Theoretical electromotive forces for cells containing a single solid or molten chloride electrolyte, J. Electrochem. Soc. 103 (1) (1956) 8–16.
[22] ASTM G1-03, Standard Practice for Preparing, Cleaning, and Evaluating Corrosion Test Specimens, 20030.10.
[23] R.P.T. Tomkins, N.P. Bansal, Gases in Molten Salts, in Solubility Data Series 45/46 Pergamon Press, 1991.
[24] H.A. Laitinen, J.A. Plambeck, Hydrogen, rhodium and iridium electrode potentials in lithium chloride-potassium chloride eutectic, JACS 87 (6) (1965) 1202–1206.
[25] J.A. Plambeck, Electromotive force series in molten salts, J. Chem. Eng. Data 12 (1) (1967) 77–82.
[26] S. Boghosian, A. Godø, H. Mediaas, T. Østvold, Oxide complexes in alkali-alkaline-earth chloride melts, Acta Chem. Scand. 45 (1991) 145–157.
[27] R.A. Skar, Chemical and Electrochemical Characterisation of Oxide/ Hydroxide Impurities in the Electrolyte for Magnesium Production (Doctoral thesis), Norwegian University of Science and Technology (NTNU), 2001.
[28] G.S. Frankel, E.A. Hughes, M.C.J. Mol, L.M. Zheludkevich, G.R. Buchheit (Eds.), Fundamentals of Corrosion Kinetics. In Active Protective Coatings: New-Generation Coatings for Metals, Springer, Dordrecht, The Netherlands, 2016.
[29] B.A.T. Mehrabadi, J.W. Weidner, B. Garcia-Diaz, M. Martinez-Rodriguez, L. Olson, S. Shimalee, Modeling the effect of cathodic protection on superalloys inside high temperature molten salt systems, J. Electrochem. Soc. 164 (4) (2017) C171–C179.
[30] B.A.T. Mehrabadi, J.W. Weidner, B. Garcia-Diaz, M. Martinez-Rodriguez, L. Olson, S. Shimpalee, Multi-dimensional modeling of nickel alloy corrosion inside high temperature molten salt systems, J. Electrochem. Soc. 163 (14) (2016) C830–C838.
[31] B.L. Garcia-Diaz, L. Olson, M. Martinez-Rodriguez, R. Fuentes, H. Colon-Mercado, J. Gray, High temperature electrochemical engineering and clean energy systems, J. South Carol. Acad. Sci. 14 (1) (2016) (Article 4).